Numerical Methods in Civil Engineering, 10-3 (2026) 25-41

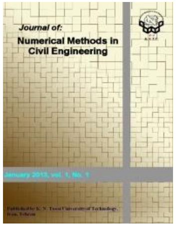

Numerical Methods in Civil Engineering

Journal Homepage: https://nmce.kntu.ac.ir/

Soil Freezing Model in the Presence of Underground Inclusion Using Hybrid Boundary-Finite Element Method

Bahman Ansari[*], **Alireza Moazzami**[**]

ARTICLE INFO

RESEARCH PAPER

Article history:
Received:
November 2025
Revised:
February 2026
Accepted:
April 2026

Keywords:
Soil Freezing
Underground Inclusion
Hybrid Solver
Boundary-Finite Element Method

Abstract:

In this study, a hybrid boundary-finite element approach is proposed for solving nonhomogeneous soil freezing models, including internal inclusions. In this regard, by dividing the nonhomogeneous model into homogeneous parts and applying the hybrid element approach to each part, the resultant equations are combined using the continuity and consistency conditions at the interface boundaries. After introducing the discretized form of the equations using hybrid element approach, the implementation is carried out in a computer code and verified by solving several classic examples. Finally, a parametric study is conducted in which a soil layer containing circular and square-shaped inclusions is modeled using the proposed method, and the effects of freezing pipes placement, inclusion geometry, and soil properties on the freezing growth performance are evaluated. The results showed that the freezing pipe configuration, combined with the inclusion geometry installed outside the inclusion, provided more uniform and optimal freezing results in comparison to other configurations make it suitable for stabilizing underground tunnel walls in a nonhomogeneous soil layer.

1. Introduction

Soil freezing is a well-known soil improvement technique, especially for temporarily stabilizing slopes, tunnel walls, or creating temporary retaining walls [1]. In practice, the effectiveness of this method largely depends on the available freezing techniques and the soil's behavior under freezing conditions. However, the initial soil conditions such as geometry, layering, material properties, and the presence of underground inclusions, are the most important parameters affecting the quality of the freezing process [2]. Due to the complex behavior of soil under freezing conditions, most studies recommend experimental and in-situ approaches as the most accurate methods for evaluating soil freezing in the field. Casini et al. (2016) proposed a constitutive effective stress model for artificial ground freezing. They validated the model by combining in-situ measurements and experimental results from natural volcanic ash samples collected during construction of the Napoli underground tunnel [3]. Hu et al. (2018) presented procedures for the study, Joudieh et al. (2024) examined how overburden pressure affects ice lens growth limitation during artificial freeze-thaw cycles in soils [5]. The study concluded that most soil properties, including density, porosity, and hydraulic conductivity, undergo significant changes during freeze-thaw cycles. Recently, the use of cold gas injection for rapid soil freezing was explained by Liu et al. (2020) and results of laboratory experiments for the range and the rate of freezing are presented in this work [6]. Despite their consistency with the physical nature of soil freezing and their ability to provide highly accurate results, in-situ methods are relatively expensive to implement and require experienced technicians and advanced equipment in practice. On the other hand, mathematical modeling and numerical methods can serve as complementary tools to in-situ approaches, enhancing efficiency while reducing implementation challenges [7]. Zhou et al. (2014) explained the application of the finite element method for solving a three-phase model consist of the soil particles, liquid water and ice lenses [8]. Alzoubi et al. (2020) conducted a comprehensive review of artificial soil freezing modelling studies, with particular emphasis on soil thermal and

---

* *Corresponding author: Department of Engineering, Faculty of Civil Engineering, University of Zanjan, Zanjan, Iran. Email:* Ansari.Bahman@znu.ac.ir

* *Department of Engineering, Faculty of Civil Engineering, University of Zanjan, Zanjan, Iran.*

https://doi.org/10.61882/NMCE.2511.1107

hydraulic properties during the freezing process. Their analysis revealed that both analytical and experimental studies in artificial ground freezing remain limited, indicating substantial opportunities for future research in this field [9]. Ren et al. (2023) developed a machine learning approach using a GA-BP neural network to estimate unfrozen water content in soils during artificial freezing. The technique was subsequently integrated into a numerical model, and the results were validated against laboratory test data [10]. Williams et al. (2024) developed a poroelastic model and numerical solution to examine ice lens formation and its impact on freezing performance during underground structure construction [11].

Numerical models such as finite element and finite difference methods are classified as volumetric approaches, requiring the discretization of the entire model domain. In contrast, the boundary element method only requires the discretization of the model boundaries, significantly reducing computational time through fewer implemented elements. Combining the features of volumetric and boundary methods, the hybrid boundary-finite element approach can be developed, by which the boundaries of the model are discretized with boundary elements and the domain of the model is discretized using a limited number of finite elements providing more accurate results [12]. In this study, the use of the boundary-finite element method (hybrid element method) is extended to solve the dynamic heat transfer equation. The method is applied to model soil freezing in a layered soil system, incorporating non-homogeneities and inclusions. In this regard, the process of applying the continuity and consistency conditions at the interface boundaries between adjacent layers is explained, and the required formulation for this purpose is derived. After validating the developed method with available analytical and semi-analytical solutions, an artificially frozen soil layer including circular and square-shaped underground inclusions are modeled and the effects of inclusion geometry, freezing pipe placement and soil properties on the freezing performance are evaluated. The results demonstrate that the proposed hybrid approach can effectively model artificial soil freezing processes under various complex conditions.

2. Methods

The main purpose of this study is to introduce a hybrid boundary–finite element approach for solving general heat-transfer equations and to use it as a tool for modeling freezing in an inhomogeneous soil medium containing underground inclusions. The flowchart of the research procedure is shown in Fig.1.

2.1. Boundary-Finite Element Method

In this section, using the weighted residual method, the heat-transfer equation is converted into its hybrid boundary–finite element form. By discretizing this formulation, a solvable form of the heat-transfer equation is obtained.

For a two-dimensional domain, the heat conduction equation, accounting for latent heat of fusion, can be expressed based on Fourier’s law [13, 25] as follows:

$$\nabla^2 T + \frac{< \nabla k, \nabla T >}{k} = \rho \frac{\sigma_{\mathrm{eff}}(T)}{k} \frac{\partial T}{\partial t} \qquad (1)$$

in which $k(x,y,t)$, $\sigma_{eff}(T)$ and ρ are the thermal conductivity, effective specific heat capacity and density, respectively and T is the temperature distribution as a function of time (t) inside the domain $\Omega(x,y)$. In Eq.1, ∇ denotes the gradient operator and $< x, y >$ represents the inner product. It should be noted that Eq.1 does not account for the effects of cryosuction, frost heave, or groundwater flow.

The effective specific heat capacity is a temperature-dependent quantity defined as follows:

$$\sigma_{eff}(T) = \begin{cases} \sigma_{cs} & T < T_f - \Delta T \\ \dfrac{L}{2\Delta T} + \dfrac{\sigma_{cs} + \sigma_{cl}}{2} & \left|T - T_f\right| < \Delta T \\ \sigma_{cl} & T > T_f + \Delta T \end{cases} \qquad (2)$$

In this equation, L is the latent heat of fusion and T_f is the freezing temperature. The parameter ΔT defines the transition range over which phase change occurs. When the temperature exceeds $T_f + \Delta T$, σ_{cl} represents the specific heat capacity of the unfrozen (saturated) soil; when the temperature falls below $T_f - \Delta T$, σ_{cs} corresponds to that of the frozen soil. Within the interval $\mid T - T_f \mid \leq \Delta T$, the specific heat capacity varies as a function of L to account for the latent heat release [25]. To avoid nonlinear complications introduced by the temperature-dependent σ_{eff}, the effective specific heat can be treated as a discrete function of temperature in the numerical scheme. This allows the governing equation to be solved separately in each thermal phase, effectively reducing it to a standard conduction equation within each defined temperature range.

Using the concept of the weighted residual method and multiplying the time-independent fundamental solutions of the static state as the weight function on both sides of the equation then integrating the resultant equations along the whole analysis domain (Ω), the following equation can be obtained:

$$\int_{\Omega} \begin{bmatrix} \nabla^2 T + \dfrac{< \nabla k, \nabla T >}{k} - \\ \rho \dfrac{\sigma_{\mathrm{eff}}(T)}{k(x,y,t)} \dfrac{\partial T}{\partial t} \end{bmatrix} . T^*(\xi, \eta, x, y) \, d\Omega = 0 \qquad (3)$$

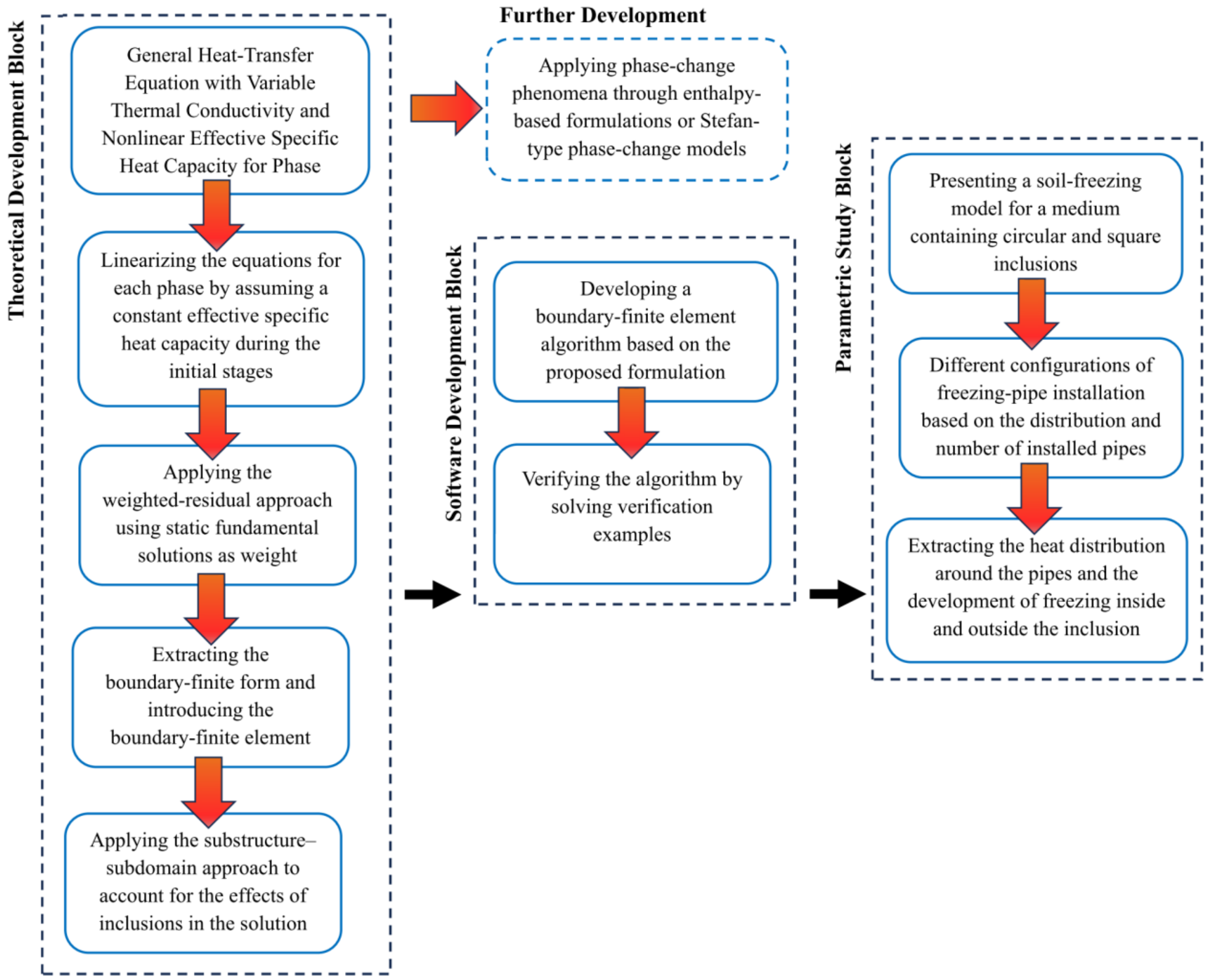

Fig. 1. Flowchart of the research procedure

where, $T^*(\xi,\eta,x,y)$, is the fundamental solution representing the temperature value of a point (x,y) due to the temperature gradient applied at the point (ξ,η). In this equation, $d\Omega$ denotes differential domain of the analysis. Applying Beti's Reciprocal theorem [14] and simplifying the resultant integrals, the following equation can be obtained:

$$c^i T(\xi,\eta,t) + \left[\int_\Gamma q^*(\xi,\eta,x,y).T\,d\Gamma - \int_\Gamma T^*(\xi,\eta,x,y).q\,d\Gamma\right] = \left[\rho\int_\Omega \frac{\sigma_{\text{eff}}(T)T^*(\xi,\eta,x,y)}{k}.\frac{\partial T}{\partial t}\,d\Omega - \int_\Omega \frac{<\nabla k,\nabla T>}{k}T^*(\xi,\eta,x,y)\,d\Omega\right] \tag{4}$$

in which $T(x,y,t)$ and $q(x,y,t)$ represents the temperature and temperature gradient ($q=\partial T/\partial \boldsymbol{n}$, $\boldsymbol{n}$: outward normal vector to the domain boundary) at point (x,y) and time t, while T^* and q^* denote the fundamental solutions for temperature and temperature gradient, respectively, within the domain Ω bounded by the boundary Γ which can be presented as follows [14, 16,17]:

$$T^* = \frac{1}{2\pi}\ln\frac{1}{\sqrt{(x-\xi)^2+(y-\eta)^2}} \tag{5}$$

$$q^* = -\frac{1}{2\pi r^2}\left[(x-\xi).n_x+(y-\eta).n_y\right] \tag{6}$$

where $r=\sqrt{(x-\xi)^2+(y-\eta)^2}$ is the distance between points (x,y) and (ξ,η), and n_x and n_y are the components of the outward normal vector to the domain boundary. In Eq.4, c^i is a constant equal to 1 for internal points and 0.5 for straight boundary elements. For other cases, it can be calculated using the rigid body movement method, as described by Brebbia and Dominguez (1992) [14] and Partridge et al. (1992) [16]. For solving Eq.4, it is assumed that the domain is discretized with NI number of three-node (triangle) elements. The temperature distribution across each element can be estimated as follows:

$$T^e(x,y) = \sum_{i=1}^{3} f_i(x,y)T_i \tag{7}$$

in which $T^e(x,y)$, is the temperature across the element e and T_i is the temperature at each element node. In this equation $f_i(x,y)$, is the shape function which can be calculated by the following:

$$f_1=\frac{x_2y_3-x_3y_2+(y_2-y_3)x-(x_2-x_3)y}{x_1y_2-x_2y_1-x_1y_3+x_3y_1+x_2y_3-x_3y_2}$$
$$f_2=\frac{x_3y_1-x_1y_3-(y_1-y_3)x+(x_1-x_3)y}{x_1y_2-x_2y_1-x_1y_3+x_3y_1+x_2y_3-x_3y_2} \tag{8}$$
$$f_3=\frac{x_1y_2-x_2y_1+(y_1-y_2)x-(x_1-x_2)y}{x_1y_2-x_2y_1-x_1y_3+x_3y_1+x_2y_3-x_3y_2}$$

where (x_i,y_i) are the coordinates of the vertex node i in the three-node element. Since the boundary of the domain is discretized with quadratic boundary elements, similar shape functions can be used to discretize the domain boundaries into boundary elements, where (x_i,y_i) represents the coordinates of the ith boundary element node [15]. Upon defining the triangular elements using Eq.7, the temperature gradient can be conveniently expressed as, $\nabla T^e=\sum_{i=1}^{3}\nabla f_i(x,y)T_i$. For simplicity, we assume that Eq.4 is applied within a single thermal phase, and the effective specific heat σ_{eff} is treated as a temperature-independent value, σ in that phase. Substituting Eq.7 into Eq.4 and discretizing the boundary and domain integrals using N_E and N_I elements, respectively, leads to the Eq.9, in which h_k^j is the kth shape function of the jth boundary element and can be calculated by Eq.8 considering (x_i,y_i) as the boundary node coordinates. If the thermal conductivity remains constant within each phase, the gradient term ∇k becomes zero, and the last integral in Eq.9 drops out. Under this condition, the matrix form of Eq.9 can be obtained by arranging the field variables from all nodes into corresponding vectors and constructing their associated coefficient matrices, as shown in Eq.10.

$$\begin{aligned}
&c^iT^i(\xi,\eta,t)+\sum_{j=1}^{NE}\int_{\Gamma_\mathrm{j}}q^*(\xi,\eta,x,y).\begin{bmatrix}h_1^j & h_2^j & h_3^j\end{bmatrix}d\Gamma_\mathrm{j}\begin{bmatrix}T_1^j\\T_2^j\\T_3^j\end{bmatrix}-\sum_{j=1}^{NE}\int_{\Gamma_\mathrm{j}}T^*(\xi,\eta,x,y).\begin{bmatrix}h_1^j & h_2^j & h_3^j\end{bmatrix}d\Gamma_\mathrm{j}\begin{bmatrix}q_1^j\\q_2^j\\q_3^j\end{bmatrix}\\
&=\sigma\rho\sum_{j=1}^{NI}\int_{\Omega_\mathrm{j}}\frac{T^*(\xi,\eta,x,y)}{k(x,y,t)}.\begin{bmatrix}f_1^j & f_2^j & f_3^j\end{bmatrix}d\Omega_\mathrm{j}\begin{bmatrix}\dot{T}_1^j\\\dot{T}_2^j\\\dot{T}_3^j\end{bmatrix}\\
&+\sum_{j=1}^{NI}\int_{\Omega_\mathrm{j}}\frac{T^*(\xi,\eta,x,y)}{k}.\begin{bmatrix}<\nabla k,\nabla f_1^j> & <\nabla k,\nabla f_2^j> & <\nabla k,\nabla f_3^j>\end{bmatrix}d\Omega_\mathrm{j}\begin{bmatrix}T_1^j\\T_2^j\\T_3^j\end{bmatrix}
\end{aligned} \tag{9}$$

$$\begin{aligned}
&\begin{bmatrix}
c^1+H_{11} & H_{12} & \cdots & H_{1(3NE)} & \cdots & 0\\
H_{21} & c^2+H_{22} & \cdots & H_{2(3NE)} & \cdots & 0\\
\vdots & \vdots & \vdots & \vdots & \vdots & \vdots\\
H_{(3NE)1} & \cdots & \cdots & c^{NE}+H_{(3NE)(3NE)} & \cdots & 0\\
\vdots & \vdots & \vdots & \vdots & \vdots & \vdots\\
H_{(3NE+3IN)1} & \cdots & \cdots & H_{(3NE+3IN)(3NE)} & \cdots & 1
\end{bmatrix}
\begin{bmatrix}T_1^B\\\vdots\\T_{3NE}^B\\T_1^I\\\vdots\\T_{3IN}^I\end{bmatrix}_{(3NE+3IN)\times 1}\\
&-\begin{bmatrix}
G_{11} & G_{12} & \cdots & G_{1(3NE)}\\
G_{21} & G_{22} & \cdots & G_{2(3NE)}\\
\vdots & \vdots & \vdots & \vdots\\
G_{(3NE)1} & \cdots & \cdots & G_{(3NE)(3NE)}\\
\vdots & \vdots & \vdots & \vdots\\
G_{(3NE+3IN)1} & \cdots & \cdots & G_{(3NE+3IN)(3NE)}
\end{bmatrix}
\begin{bmatrix}q_1^B\\.\\.\\q_{3NE}^B\end{bmatrix}_{3NE\times 1}\\
&=\begin{bmatrix}
I_{11} & I_{12} & \cdots & I_{1(3NE+3IN)}\\
I_{21} & I_{22} & \cdots & I_{2(3NE+3IN)}\\
\vdots & \vdots & \vdots & \vdots\\
I_{(3NE+3IN)1} & \cdots & \cdots & I_{(3NE+3IN)(3NE+3IN)}
\end{bmatrix}
\begin{bmatrix}\dot{T}_1^B\\\vdots\\\dot{T}_{3NE}^B\\\dot{T}_1^I\\\vdots\\\dot{T}_{3IN}^I\end{bmatrix}_{(3NE+3IN)\times 1}
\end{aligned} \tag{10}$$

In Eq.10, T_i^B and T_j^I represent the temperature at the ith boundary node and jth internal point, respectively, while q_i^B denotes the temperature gradient at boundary node i. The elements of coefficient matrices H_{ij}, G_{ij} and I_{ij} can be calculated by applying numerical integration across each boundary and domain elements as follows:

$$\begin{cases}
H_{ij}=\int_{\Gamma_{\lceil\frac{j}{3}\rceil}}q^*(\xi_i,\eta_i,x,y).\,h_{\left(j-3\left(\lceil\frac{j}{3}\rceil-1\right)\right)}^{\lceil\frac{j}{3}\rceil}\,d\Gamma_{\lceil\frac{j}{3}\rceil}\\
G_{ij}=\int_{\Gamma_{\lceil\frac{j}{3}\rceil}}T^*(\xi_i,\eta_i,x,y).\,h_{\left(j-3\left(\lceil\frac{j}{3}\rceil-1\right)\right)}^{\lceil\frac{j}{3}\rceil}\,d\Gamma_{\lceil\frac{j}{3}\rceil}\\
I_{ij}=\frac{\sigma\rho}{k}\int_{\Omega_{\lceil\frac{j}{3}\rceil}}T^*(\xi_i,\eta_i,x,y).\,f_{\left(j-3\left(\lceil\frac{j}{3}\rceil-1\right)\right)}^{\lceil\frac{j}{3}\rceil}\,d\Omega_{\lceil\frac{j}{3}\rceil}
\end{cases} \tag{11}$$

in which, $\lceil x \rceil$ is the ceiling function; superscript for h and f, denote the element number and subscript represents the function number which can be selected as 1,2 or 3; $\left\lceil \frac{j}{3} \right\rceil$ represents both the element number for each shape function and the subdomain number, $\Omega_{\lceil j/3 \rceil}$. As shown in Eq.10, the coefficient c^i equals 1 for internal points and 0.5 for both straight-connected boundary elements and middle nodes of quadratic elements. For other boundary nodes, this value can be calculated using the known angle θ between two adjacent boundary elements, using following equation [14, 16, 17]:

$$c^i = \frac{\theta}{2\pi} \tag{12}$$

Alternatively, the coefficient c^i can be determined using the rigid body movement method [14]. It is possible to represent the Eq.10 in a more compact form as follows:

$$[H]\{T\} + [G]\{q\} = [I]\{\dot{T}\} \tag{13}$$

In which $[H]$, $[G]$ and $[I]$ represent coefficient matrices, while $\{T\}$, $\{q\}$ and $\{\dot{T}\}$ are vectors containing all nodal variables from Eq.10. The final solvable form of equation (Eq.13) can be obtained by discretizing the time axis into $NSTEP$ time steps of length Δt. Various methods, such as the backward difference [18], Newmark-Beta [19], and Houbolt [20] methods, have been proposed for this purpose. However, after evaluating these approaches, the backward difference method demonstrated greater stability and accuracy compared to the others when solving Eq.13. The backward difference discretization can be implemented as follows:

$$\{\dot{T}\}_{t+\Delta t} = \frac{\{T\}_{t+\Delta t} - \{T\}_t}{\Delta t} \tag{14}$$

in which $\{T\}_{t+\Delta t}$ and $\{T\}_t$ are the temperature values at preceding time steps $t + \Delta t$ and t, respectively. The hybrid formulation presented in Eq.13 offers two main advantages compared to the traditional Dual Reciprocity Boundary Element Method (DRBEM) and conventional boundary-finite element approaches. First, the use of higher-degree internal elements in the proposed method significantly reduces the number of internal points required in the DRBEM. This allows complex problems to be modeled with fewer internal points, improving computational efficiency. Second, the new hybrid approach integrates boundary and finite element concepts into a unified scheme. In contrast, traditional boundary-finite element methods apply each formulation separately to the model and combine the results only at the final solution stage within a single matrix. The proposed hybrid framework streamlines this process, making it simpler to model complex geometries and physical conditions.

2.2. Freezing Model Around the Underground Inclusions

Fig.2 presents a two-dimensional, underground inclusion and pre-installed freezing pipes within a soil layer. Based on this figure, extracting a solvable hybrid solution for this model requires dividing the nonhomogeneous model into two distinct homogeneous models. The first model consists of the soil layer with an empty space, and the second model considers a homogeneous inclusion with pre-installed freezing pipes. Using the hybrid approach concept presented in the previous section, the solvable matrix for the first model can be expressed as follows:

$$\begin{bmatrix} H_\Omega & H_\Omega^{inter} \end{bmatrix} \begin{Bmatrix} T_\Omega \\ T_\Omega^{inter} \end{Bmatrix} + \begin{bmatrix} G_\Omega & G_\Omega^{inter} \end{bmatrix} \begin{Bmatrix} q_\Omega \\ q_\Omega^{inter} \end{Bmatrix} = [I_\Omega]\{\dot{T}_\Omega\} \tag{15}$$

in which T_Ω and q_Ω are the temperature and temperature gradient for the nodes inside the domain Ω, and T_Ω^{inter} and q_Ω^{inter} are the temperature and temperature gradient on the interface boundary nodes, Γ^{inter} of the domain. H_Ω, H_Ω^{inter}, G_Ω, G_Ω^{inter} and I_Ω, are the corresponding coefficient matrices, which can be calculated using Eq.11 while considering only domain Ω of the first model. Similarly, for the second model, the following equation can be obtained:

$$\begin{bmatrix} H_{\Omega'} & H_{\Omega'}^{inter} \end{bmatrix} \begin{Bmatrix} T_{\Omega'} \\ T_{\Omega'}^{inter} \end{Bmatrix} + \begin{bmatrix} G_{\Omega'} & G_{\Omega'}^{inter} \end{bmatrix} \begin{Bmatrix} q_{\Omega'} \\ q_{\Omega'}^{inter} \end{Bmatrix} = [I_{\Omega'}]\{\dot{T}_{\Omega'}\} \tag{16}$$

In the above equation, all nodal variables can be defined using the same formulation as in the first model, with the only difference being that the analysis domain is now Ω'. Since temperature and flux distributions must be continuous and consistent at the interface boundaries, respectively, the following equation must be satisfied:

$$\begin{cases} T_\Omega^{inter} = T_{\Omega'}^{inter} \\ -k_\Omega q_\Omega^{inter} - k_{\Omega'} q_{\Omega'}^{inter} = 0 \end{cases} \tag{17}$$

where k_Ω and $k_{\Omega'}$, are the thermal conductivity of domains Ω and Ω' ,respectively. Finally, by combining Eq.15, Eq.16 and Eq.17, the solvable form of the equations can be presented as follows:

$$\begin{bmatrix} H_\Omega & H_\Omega^{inter} & 0 \\ 0 & H_{\Omega'}^{inter} & H_{\Omega'} \end{bmatrix} \begin{Bmatrix} T_\Omega \\ T_\Omega^{inter} \\ T_{\Omega'} \end{Bmatrix} + \begin{bmatrix} G_\Omega & G_\Omega^{inter} & 0 \\ 0 & -\frac{k_\Omega}{k_{\Omega'}} G_{\Omega'}^{inter} & G_{\Omega'} \end{bmatrix} \begin{Bmatrix} q_\Omega \\ q_\Omega^{inter} \\ q_{\Omega'} \end{Bmatrix} = \begin{bmatrix} I_\Omega & 0 \\ 0 & I_{\Omega'} \end{bmatrix} \begin{Bmatrix} \dot{T}_\Omega \\ \dot{T}_{\Omega'} \end{Bmatrix} \tag{18}$$

in which, the values of coefficient matrices with superscript "*inter*" are only calculated once for the interface boundaries. As shown in Fig.2, the boundary conditions assume a known temperature of $T = 21\ ^oC$ at the surface boundary and a zero-flux condition ($-kq = 0$) on all side boundaries, representing the semi-infinite soil layer configuration. Additionally, freezing pipes are included in the model, with a prescribed temperature boundary condition of $T = 0\ ^{o}C$.

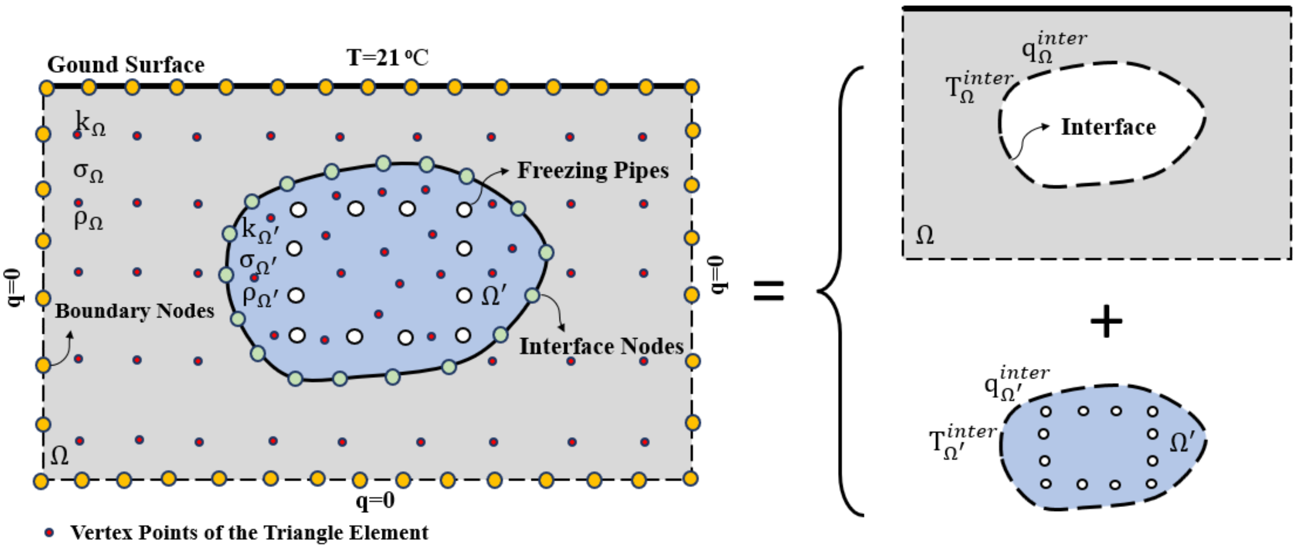

Fig. 2. Decomposition of a nonhomogeneous soil layer into the two separate homogeneous layers using hybrid boundary-finite element method

2.3. Verification

The methods and formulations presented in the previous sections are implemented in a computer code called HybSol (**Hyb**rid **Sol**ver). This code can generate and account for complex geometries and nonhomogeneous materials during the solution process. In this section, the code is validated by solving several classic examples with known analytical responses. In the first example, a square plate is considered with an initial temperature of $T_0 = 30\ ^{0}C$ across its surface, cooled with a thermal shock, $T_0 = 0\ ^{0}C$ at its side boundaries. It should be noted that this problem was solved using 4 quadratic boundary elements (with 8 nodes) and 8 internal elements. For the volumetric discretization, only a single internal point was placed at the center of the square. The analysis was carried out over 25 time steps, each with a step size of 0.1 s. The total computation time using the hybrid approach was approximately 1 second. Bruch and Zyvoloski (1974) provided an analytical solution for the temperature variation at the center of the plate [21]. Fig.3(a) compares the HybSol results with the analytical solution. As shown in the figure, the results are in excellent agreement. In the second example, the results of temperature variation on the boundaries of a square plate with initial temperature $T_0 = 1\ ^{0}C$ cooled with thermal shock from the side boundaries is evaluated. This example is important because it allows the reliability of results to be evaluated at boundary points and geometric edges, where flux tends toward infinity. All geometric and material properties for this case are provided in Fig.3(b). Similar to the previous example, 4 boundary elements (with 8 nodes) and 8 internal triangular elements (with 1 internal point for volumetric discretization) are used. The simulation is performed over 25 time steps with a step size of 0.06 s. Using the hybrid approach, the computation time is approximately 1 second. Additionally, this figure compares the results of HybSol with the analytical solution from Wrobel et al. (1986) [22] at three boundary points of the plate. As can be seen again there is a great agreement between solutions. In the third example, an oval-shaped plate with an initial temperature $T_0 = 0\ ^{0}C$ is warmed by maintaining boundaries at $T_0 = 1\ ^{0}C$. The analytical solution for temperature variation at the oval's center point was presented by Wrobel et al. (1986) [23]. The oval-shaped geometry example is significant because it allows the accuracy of temperature variation predictions around curved (quadratic) geometries to be assessed. In this case, the model employs 8 quadratic boundary elements (with 16 nodes) and 16 internal triangular elements, using a single internal point at the center of the oval for volumetric discretization. It should be noted that the simulation was carried out over 30 time steps, each with a step size of 0.05 s. The total computation time for this example was approximately 5 seconds. Fig.3(c) compares the HybSol results with both analytical and finite element solutions, demonstrating the accuracy of the proposed method relative to other approaches.

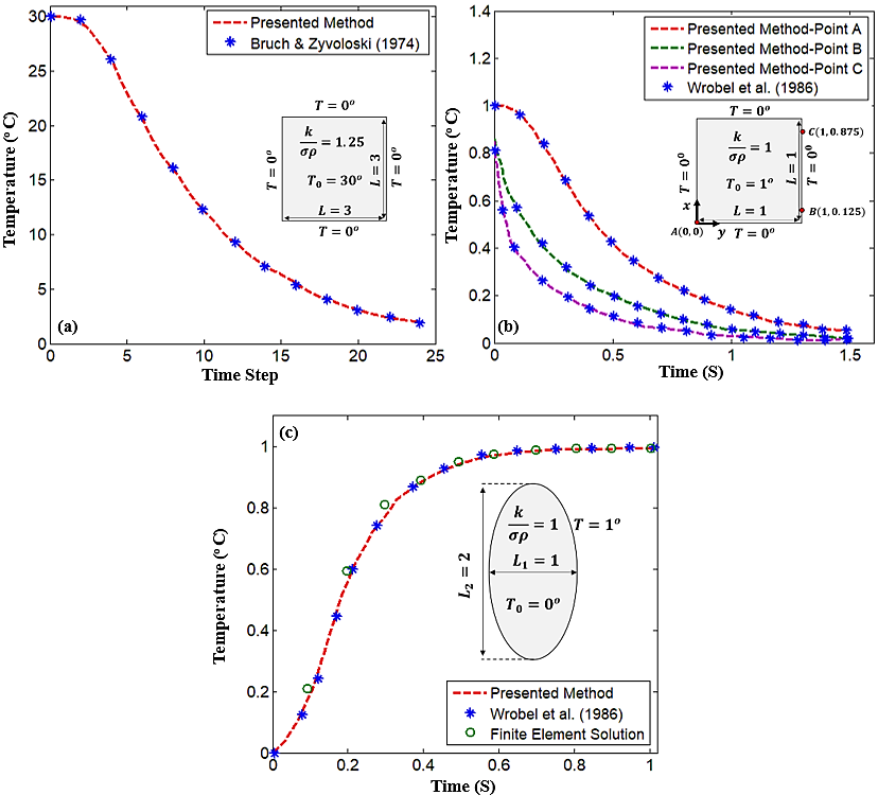

Fig. 3. Comparing the results of HybSol (Hybrid Solver) code with analytical and other numerical solutions a) Temperature variation at the center of square plate subjected to thermal shock; b) Temperature variation at the boundaries of the square plate subjected to thermal shock; c) Temperature variation at the center of oval shaped plate subjected to thermal shock.

3. Parametric Study

In this section, a soil layer containing internal inclusions with circular and square geometries is examined under different conditions. In the first scenario, the soil layer is composed of saturated Kaolin clay, while the inclusion consists of saturated Ottawa sand soil. This condition is analyzed to evaluate the effects of inclusion geometry and freezing pipe placement on freezing performance. In the second scenario, the soil layer is composed of saturated Ottawa sand, and the inclusion consists of saturated Kaolin clay. The same parameters are assessed to conduct a comparative study, aiming to determine the optimal location and configuration for installing freezing pipes in the presence of internal inclusions.

3.1. *Sand Inclusion within Clay Soil*

In the first example, a saturated Kaolin clay layer containing an inclusion of saturated Ottawa sand is considered. Based on experimental data, Carpenter (2019) [24] provided the thermal properties of clay and sand soil layers under varying conditions. From this work, the thermal properties of the soil layer and inclusion can be extracted for saturated clay and sand at specific environmental temperatures and initial relative densities. In this study, saturated Kaolin clay and Ottawa sand are considered for the soil layer and inclusion, respectively. The thermal properties of each material are presented in Table 1. Additionally, Fig.4 shows the geometrical and thermal properties of each model. Based on this figure, the inclusion geometry is assumed to be both circular and square, with side length/diameter $a = 20m$, while the freezing pipe diameter is assumed to be $d_p = 1m$. The freezing pipes are installed in two different configurations. In the first configuration, the pipes are placed inside the inclusion. In the second configuration, they are installed outside the inclusion (within the surrounding soil layer). The pipes are geometrically distributed in the soil layer following the same pattern as the inclusion's geometry. However, the spacing between pipes varies according to the distribution constant parameter, defined as follows:

$$\varphi = \frac{D}{P} \tag{19}$$

where D is the minimum distance between adjacent pipes (in meters), and P is the perimeter of the pipe distribution geometry (in meters). A higher φ value indicates a smaller number of pipes installed within a given distance. For square inclusion, the distribution constant varies in two cases, $\varphi = 0.0625$ and $\varphi = 0.125$. These values apply to both inside and outside pipe installations. Similarly, for circular inclusion, the distribution constant is $\varphi = 0.120$ and $\varphi = 0.240$. The soil's surface boundary is assumed to have a fixed normal temperature of $T = 21\ ^{o}C$. Since the side boundaries are connected to an adjacent soil layer of the same material, the temperature gradient at these boundaries is assumed to be fixed and equal to zero ($q = 0$). Additionally, the freezing pipe boundaries are treated as having a constant temperature of $T = 0\ ^{o}C$ over time. The model is solved using 30 quadratic boundary elements to discretize the side boundaries and the ground surface. In addition, 5 quadratic elements are employed for each freezing pipe, and 20 quadratic elements are used to discretize each inclusion boundary. The domain is discretized using 60 triangular elements, with locally dense element between the freezing pipes and inclusion and by going far from them the element density decreased by a factor of 0.5 for each 3 meters. As example are solved with 500 time-steps with step length 0.01 day (864 seconds). It is worth noting that all models are solved with hybrid approach in 48 seconds computation time. the most time-consuming part of the calculation was the inverse of coefficient matrix of Eq.18 which took 25 seconds, then the calculation of temperature in each step only took around 0.05 seconds.

Table 1. Thermal Properties of soil Layer and inclusion [24]

Soil Layer	Relative Density (%)	Environment Temperature (C)	Density (Kg/m^3)	Thermal Conductivity (W/mC)	Specific Heat Capacity (J/KgC)
Kaolin Clay	-	21	1900	1.6	1400
Ottawa Sand	80	21	2148	3	1300

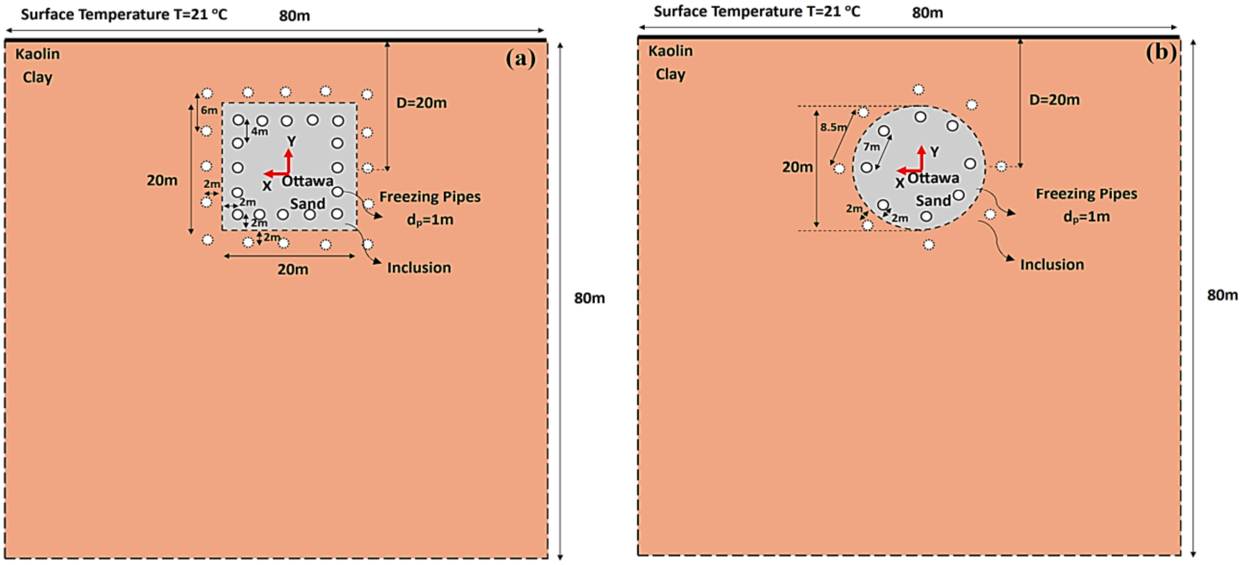

Fig. 4. Geometrical configuration of installed freezing pipes inside a soil layer a) Square type configuration; b) Circular type configuration. In both cases, the freezing pipes are installed either inside or outside the inclusion separately.

Fig.5 shows the temperature distribution on the left side of the circular-type inclusion as a function of time and distance from the inclusion's center. Figs.5(a) and 5(b) present the results for freezing pipes located inside and outside the inclusion, respectively, with a distribution constant of $\varphi = 0.240$ in both cases. Based on these figures, when the pipes are inside the inclusion, the temperature at points located in the center reaches $T = 5\ ^{o}C$ after 5 days. When the pipes are outside the inclusion, the temperature decreases uniformly throughout all points interior the inclusion, reaching an average value of $T = 10\ ^{o}C$ after 5 days. For points exterior the inclusion when pipes are installed inside it, the temperature increases steadily from $T = 10\ ^{o}C$ near the inclusion boundary to $T = 21\ ^{o}C$ at a distance of $X = 1.4a$ from the inclusion center. This finding demonstrates that the freezing performance in this case is not particularly significant, especially for points exterior the inclusion. When pipes are installed outside the inclusion, both interior and exterior points experience more significant freezing effects, with temperatures reaching $T = 2\ ^{o}C$ at a distance of $X = 0.7a$ from the inclusion center. When decreasing the distribution constant to $\varphi = 0.120$ in Figs.5(c) and 5(d), the temperature drops more rapidly. Points within the inclusion reach $T = 0\ ^{o}C$ after just 2 days when pipes are placed within it. However, for exterior points, the freezing effect differs slightly from that shown in Fig.5(a) with $\varphi = 0.240$. A similar effect occurs when pipes are installed outside the inclusion. The temperature decreases uniformly throughout the interior points, reaching $T = 5\ ^{o}C$ after 5 days. For exterior points in this configuration, however, the temperature drops more rapidly and propagates farther compared to the $\varphi = 0.240$ case.

Fig.6 shows the temperature distribution for a square-type sand inclusion embedded within a clay soil layer. Fig.6(a) and Fig.6(b) present the temperature distribution on the left side of the inclusion for $\varphi = 0.125$. As shown, the temperature drops to zero after 3 days for most points interior the inclusion when freezing pipes are installed within it. It is possible to directly compare the results of the previous circular-type inclusion (for $\varphi = 0.125$) with this case ($\varphi = 0.120$). As seen in Figs.5(c) and 6(a), both cases exhibit similar performance for interior points. However, for exterior points, the square configuration yields better results, with temperatures reaching lower values compared to the circular configuration. In other words, for points exterior the inclusion, the freezing effect extends over longer distances. After 4 days, the point at $X = 0.6a$ reaches a temperature below $T = 7\ ^oC$ in Fig.6(a). By contrast, in the earlier case with a circular inclusion (Fig.5(c)), the temperature fell below $T = 10\ ^oC$ over the same period. Additionally, when pipes are installed outside the inclusion, the interior points cool more uniformly than in the circular inclusion case, and the temperature distributions are more tightly clustered for all evaluated interior points. When the distribution constant decreases to $\varphi = 0.0625$, in Fig.6(c) and Fig.6(d), it is clearly evident that the interior points rapidly cool to $T = 0\ ^oC$ within just 3 days. Moreover, this effect occurs uniformly across all points when the freezing pipes are installed inside the inclusion. A similar effect occurs when the pipes are placed outside the inclusion. However, in this configuration, all interior points uniformly cool to $T = 2\ ^oC$ after 6 days. For exterior points when pipes are installed outside the inclusion, freezing develops more rapidly, with temperatures reaching $T = 0\ ^oC$ at a distance of $X = 0.7a$ within 5 days. The result is consistent with the circular inclusion case.

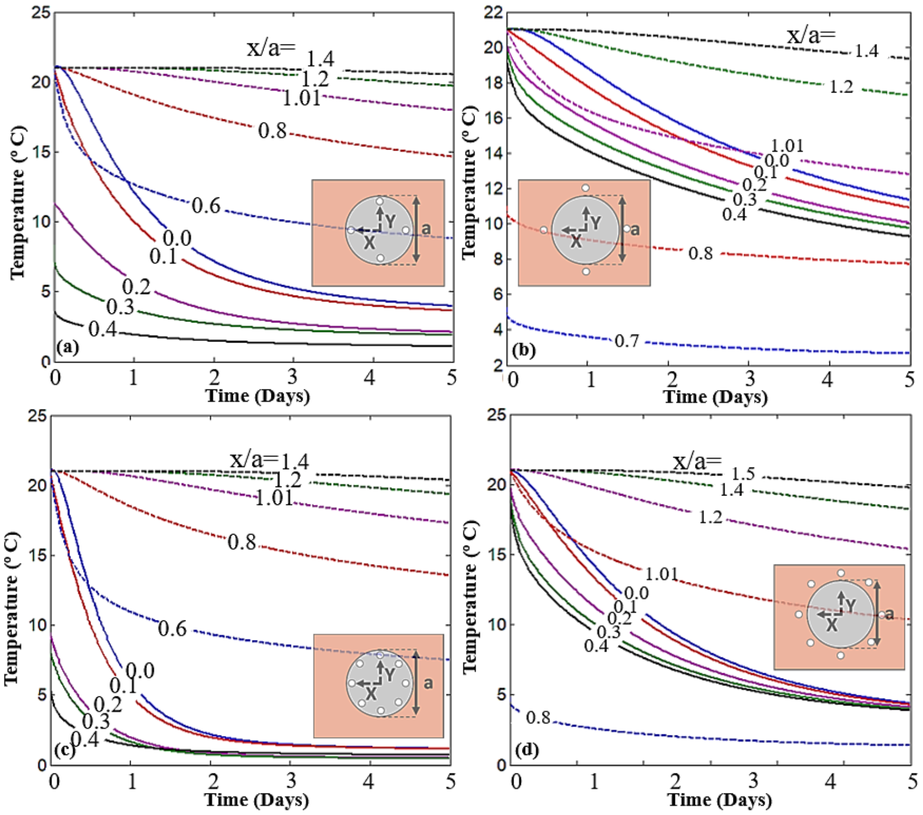

Fig. 5. Temperature distribution along the left boundary of the circular Ottawa sand inclusion and Kaolin clay soil layer when freezing pipes are installed a) inside inclusion with $\varphi = 0.240$; b) outside inclusion with $\varphi = 0.240$; c) inside inclusion with $\varphi = 0.120$; d) outside inclusion with $\varphi = 0.120$

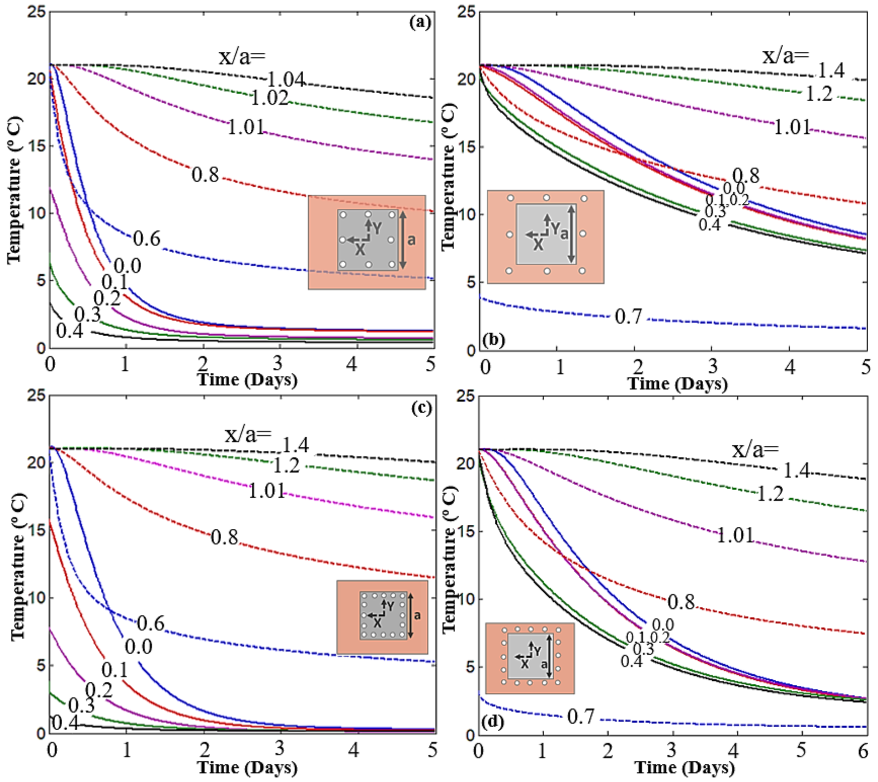

Fig. 6. Temperature distribution along the left boundary of the square Ottawa sand inclusion and Kaolin clay soil layer when freezing pipes are installed a) inside inclusion with $\varphi = 0.125$; b) outside inclusion with $\varphi = 0.125$; c) inside inclusion with $\varphi = 0.0625$; d) outside inclusion with $\varphi = 0.0625$.

Fig.7 shows the snapshot of temperature distribution in a circular inclusion with a distribution constant of $\varphi = 0.240$. Note that each time step in the figure represents 0.01 days, where darker regions indicate colder temperatures and lighter red areas correspond to the warmest points ($T = 21\ ^{o}C$). As shown in Fig.7(a), when pipes are installed inside the inclusion, the interior points freeze rapidly, and their temperature drops below $T = 10\ ^{o}C$. In contrast, Fig.7(b) demonstrates that when pipes are installed outside the inclusion, the freezing process is slower and only the areas near the pipes reach temperatures below $T = 10\ ^{o}C$ in same duration of time. Fig.8(a) shows temperature snapshots for a distribution constant of $\varphi = 0.120$. As illustrated, the freezing zone inside the inclusion expands rapidly, with interior points dropping below $T = 10\ ^{o}C$. A ring-shaped area forms at the center of the inclusion, where temperatures reach $T = 0\ ^{o}C$, while adjacent points remain at higher temperatures during the same period. When the pipes are installed outside the inclusion (Fig.8(b)), the interior of the inclusion still experiences temperatures below $T = 10\ ^{o}C$ after 5 days. However, points exterior the inclusion near the pipes also cool to this temperature within the same period.

Fig.9 and Fig.10 present snapshots of the temperature changes for the square-type inclusion. Based on Fig.9(a), when pipes with $\varphi = 0.125$ are installed inside the inclusion, the temperature decreases rapidly within the inclusion, dropping below $T = 2\ ^{o}C$ after 5 days. Based on Fig.9(a), temperatures at points exterior to the inclusion drop below $T = 10\ ^{o}C$ near its boundary. When the pipes are installed outside the inclusion (Fig.9(b)), the temperature decreases uniformly for both interior and exterior points. However, the temperature drop is lower compared to internal pipe installation, particularly for points inside the inclusion. According to Fig.10(a), when the distribution constant is $\varphi = 0.0625$, all points inside the inclusion reach $T = 0\ ^{o}C$ within three days, and the affected area outside the inclusion is larger than in the previous case. When pipes are installed outside the inclusion (Fig.10(b)), the temperature decreases nearly uniformly for all points, both inside and outside. However, the freezing rate inside the inclusion is slightly slower than outside, with all points dropping below $T = 5\ ^{o}C$ after 5 days of freezing.

Fig.11(a) presents temperature distributions when circular freezing pipes ($\varphi = 0.120$) are installed inside a square inclusion. Fig.11(b) shows freezing progression for a circular inclusion with a square freezing pipe configuration ($\varphi = 0.0625$). In both cases, the freezing pattern follows the pipe configuration. In the first case, the freezing performance is non-uniform. Compared to previous cases, the temperature difference at the edges of the square inclusion is significantly higher than at its center. In contrast, when the freezing pipe configuration matches the inclusion geometry (as in previous cases), more uniform results are achieved. Similar patterns are observed in Fig.11(b). However, when freezing pipes are installed outside the inclusion, all interior points freeze uniformly, and the freezing radius extends significantly beyond the inclusion boundaries.

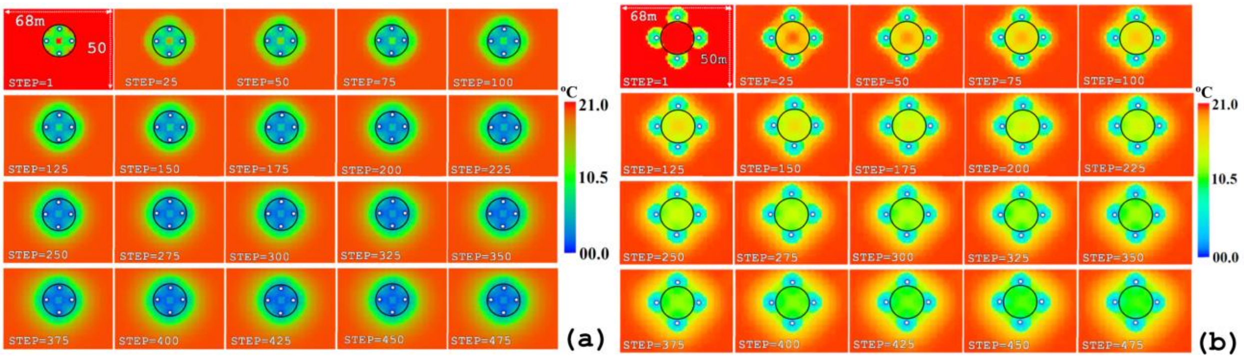

Fig. 7. Snapshot of thermal distribution inside Kaolin clay soil layer and circular type Ottawa sand inclusion with $\varphi = 0.240$ when freezing pipes are installed a) inside inclusion; b) outside inclusion. The step length is 0.01 day.

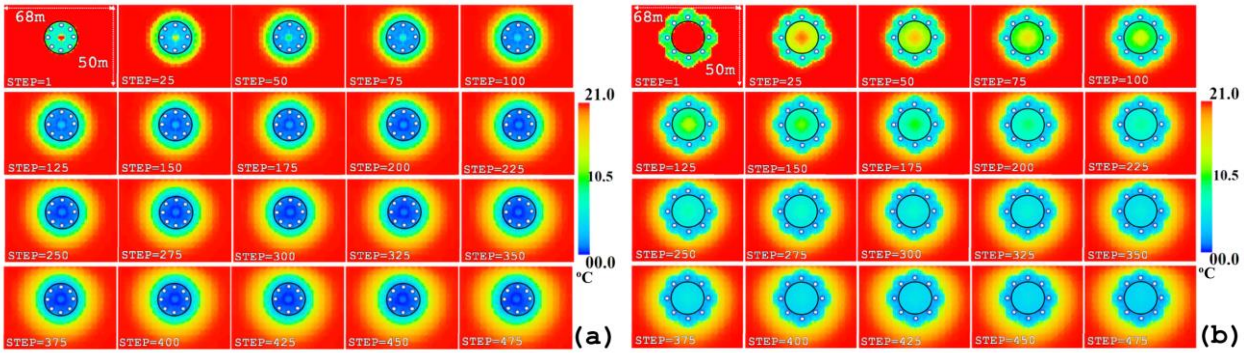

Fig. 8. Snapshot of thermal distribution inside Kaolin clay soil layer and circular type Ottawa sand inclusion with $\varphi = 0.120$ when freezing pipes are installed a) inside inclusion; b) outside inclusion. The step length is 0.01 day.

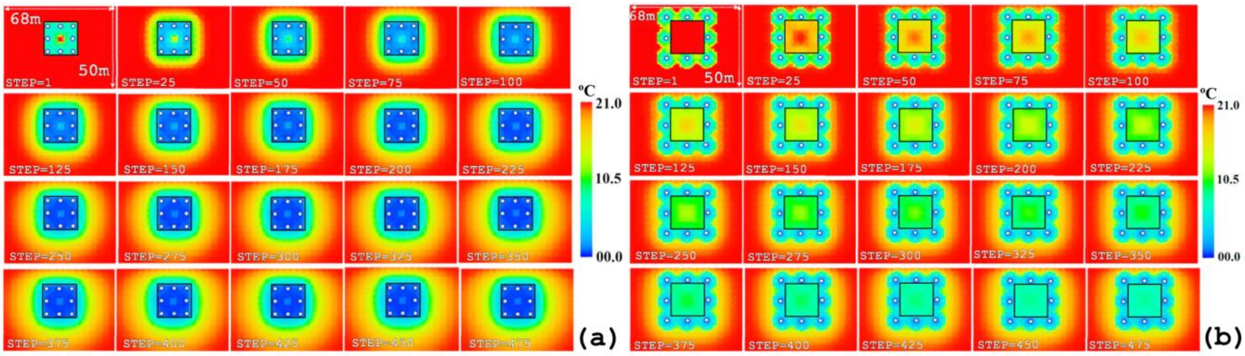

Fig. 9. Snapshot of thermal distribution inside Kaolin clay soil layer and square type Ottawa sand inclusion with $\varphi = 0.125$ when freezing pipes are installed a) inside inclusion; b) outside inclusion. The step length is 0.01 day.

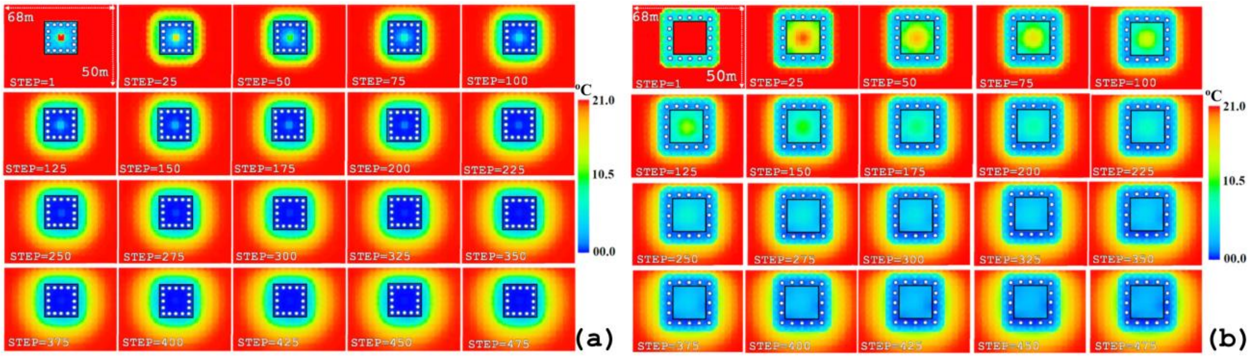

Fig. 10. Snapshot of thermal distribution inside Kaolin clay soil layer and square type Ottawa sand inclusion with $\varphi = 0.0625$ when freezing pipes are installed a) inside inclusion; b) outside inclusion The step length is 0.01 day.

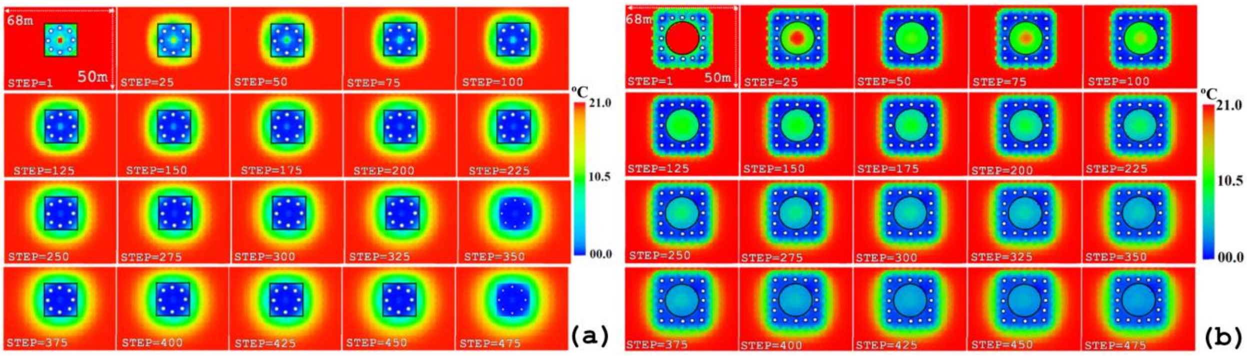

Fig. 11. Snapshot of thermal distribution inside Kaolin clay soil layer and Ottawa sand inclusion a) Square type inclusion-circular pipe configuration inside the inclusion, $\varphi = 0.120$; b) Circular type inclusion-square pipe configuration outside the inclusion, $\varphi = 0.0625$. The step length is 0.01 day.

In summary, for both circular and square inclusions where the soil layer consists of Kaolin clay and the inclusion is sand-based, uniform temperature fall occurs both inside and outside the inclusion when pipes are installed externally. However, the time required to fully freeze interior points increases compared to internal pipe installation. Optimal freezing performance is achieved when the pipe configuration matches the inclusion's geometry.

3.2. Clay Inclusion within Sandy Soil

In the second example, it is assumed that the inclusion is the type of saturated Kaolin clay, and the soil layer consists of saturated Ottawa sand. The thermal properties of each layer are identical to those in Table 1. The results are presented for both square and circular shaped inclusions with the same freezing pipe configuration and distribution constant as seen in the previous example. Fig.12 presents the temperature distribution on the left side of the circular type inclusion with $\varphi = 0.240$. Based on Fig.12(a), when pipes are installed inside the inclusion, the freezing process is slower compared to the previous example. This is because the thermal diffusivity of clay is lower than that of sand. However, the center of inclusion reaches to below $T = 10\ ^oC$ after 5 days. In contrast, exterior points experience almost the same situation as seen in the previous example and the speed of freezing remains unchanged for this case. When pipes are installed outside the inclusion in Fig.12(b), the temperature decreases uniformly for interior points and averages to a value of $T = 12\ ^oC$ after 5 days. In exterior points near the freezing spots $X = 0.7a$, the temperature reaches below $T = 2\ ^oC$ after 5 days, however, by moving away from spot the freezing performance rapidly decreases. When the distribution constant is $\varphi = 0.240$ (Fig.12(c)), the freezing rate increases, and the temperature at all points interior to the inclusion reaches near-zero values only after 2 days. However, compared to the previous case (Fig.5), the freezing rate in this case is 5% slower. When the pipes are outside the inclusion (Fig.12(d)), the temperature at all evaluated points drops below $T = 5\ ^oC$on average after 5 days. Additionally, points near the pipes at $X = 0.7a$ experience temperatures below $T = 2\ ^oC$ within 2 days in this configuration.

If the inclusion geometry is assumed to be square-shaped, the temperature distribution inside and on the left side of the inclusion is presented in Fig.13. Based on Fig.13(a), when freezing pipes are installed inside the inclusion with a distribution constant of $\varphi = 0.125$, the temperature values drop below $T = 5\ ^oC$ after 5 days for all interior points. Compared to the equivalent circular inclusion in Fig.12(c), this process is slower. The circular configuration achieves temperatures below $T = 5\ ^oC$ for most interior points in just 3 days. However, for exterior points, the square-type inclusion demonstrated better performance, achieving lower temperatures at greater distances compared to the circular-type. When freezing pipes are installed outside the inclusion (Fig.13(b)), the square-type configuration demonstrates better performance than the circular type (Fig.12(d)) for interior points, as all evaluated points exhibit a uniform temperature drop. For exterior points as well, the square-type configuration in Fig.13(b) shows better performance compared to the circular type, achieving lower temperatures at greater distances. Increasing the number of installed pipes in Fig.13(c) with $\varphi = 0.0625$ results in a slightly improved freezing rate, particularly for points at the center of the inclusion. However, for other points, the performance remains nearly identical to that in Fig.13(a). When pipes are installed outside the inclusion in Fig.13(d), both interior and exterior points experience a lower and more uniform temperature distribution compared to Fig.13(b).

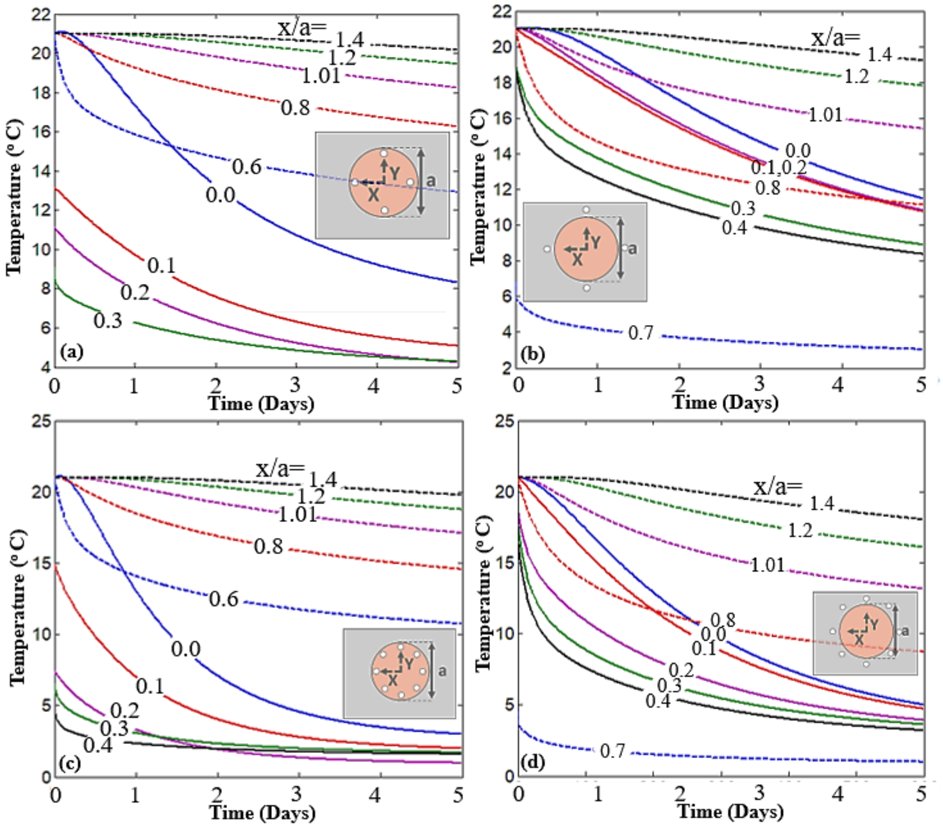

Fig. 12. Temperature distribution along the left boundary of the circular Kaolin clay inclusion and Ottawa sand soil layer when freezing pipes are installed a) inside inclusion with $\varphi = 0.240$; b) outside inclusion with $\varphi = 0.240$; c) inside inclusion with $\varphi = 0.120$; d) outside inclusion with $\varphi = 0.120$.

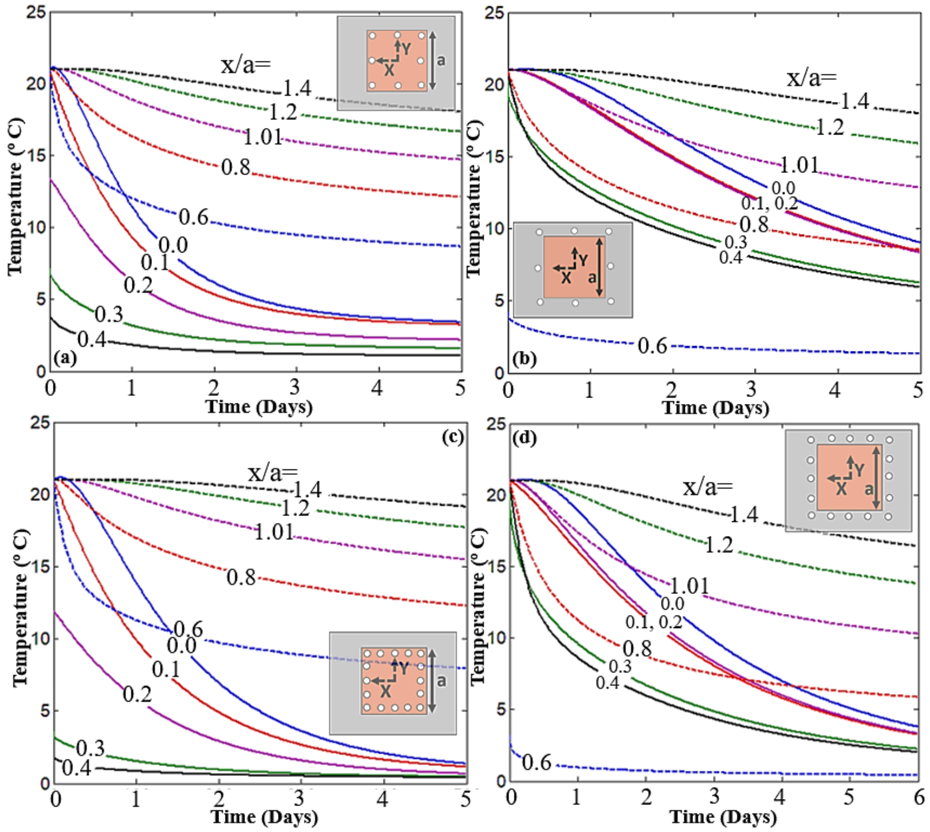

Fig. 13. Temperature distribution along the left boundary of the square Kaolin clay inclusion and Ottawa sand soil layer when freezing pipes are installed a) inside inclusion with $\varphi = 0.125$; b) outside inclusion with $\varphi = 0.125$; c) inside inclusion with $\varphi = 0.0625$; d) outside inclusion with $\varphi = 0.0625$.

Figs.14 to 17 present snapshots of temperature changes inside and around the clay inclusion embedded in the sand layer for different freezing pipe configurations. It can be observed that when the pipes are installed inside the inclusion, the freezing rate and performance are more effective for interior points. This performance further improves when more pipes are used in the freezing process. In contrast, for the exterior points, the freezing rate is lower than for the interior points. However, in this case, the freezing performance is more effective, and the freezing extends over greater distances compared to the previous example with a sand inclusion and clay soil layer. When pipes are installed outside, the inclusion freezing process covers both internal points and exterior points uniformly. It is observed that both circular and square pipe configurations exhibit uniform freezing performance in this case. Fig.18(a) presents the temperature distribution results for a square-type inclusion with circular pipe installation configuration. As shown in the figure, the freezing front develops according to the pipe configuration pattern, while the edges of the square inclusion do not reach lower temperatures relative to adjacent points even after 5 days. Similar results are observed in Fig.18(b) for the circular-type inclusion with square pipe configuration installed outside the inclusion. The key difference is that all exterior points experience a rapid temperature drop, while interior points uniformly reach freezing temperature.

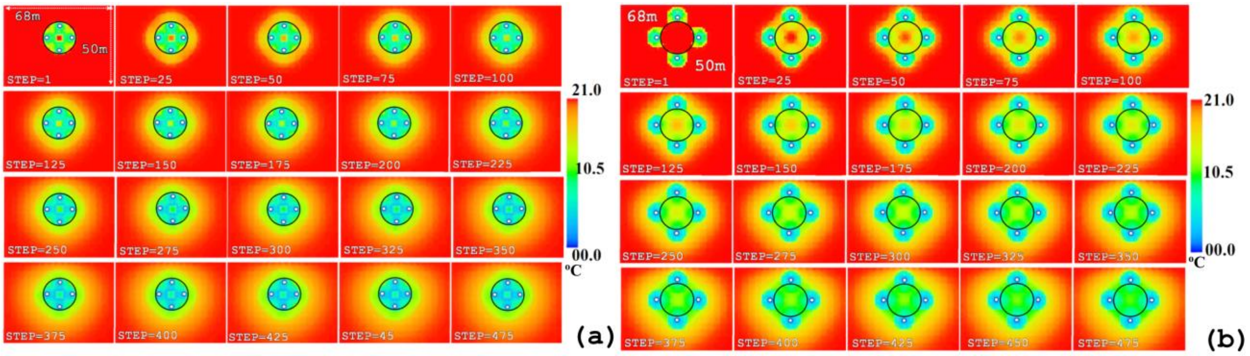

Fig. 14. Snapshot of thermal distribution inside Ottawa sand soil layer and circular type Kaolin clay inclusion with $\varphi = 0.240$ when freezing pipes are installed a) inside inclusion; b) outside inclusion. The step length is 0.01 day.

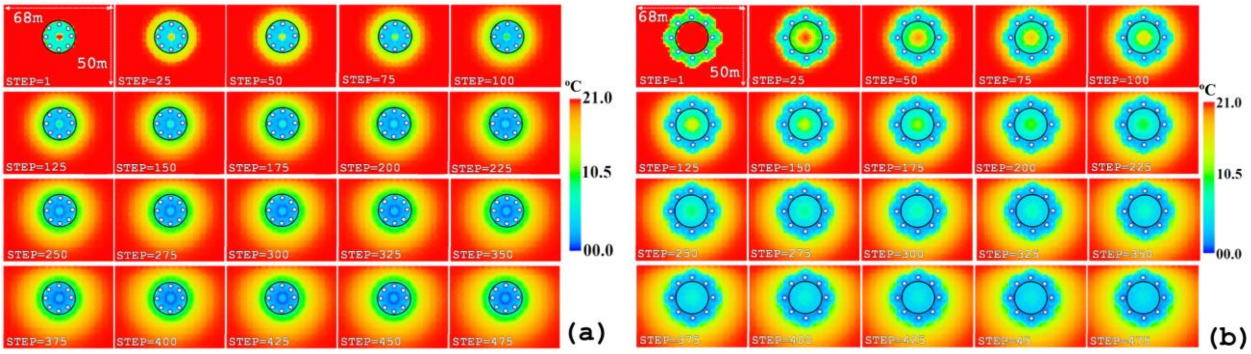

Fig. 15. Snapshot of thermal distribution inside Ottawa sand soil layer and circular type Kaolin clay inclusion with $\varphi = 0.120$ when freezing pipes are installed a) inside inclusion; b) outside inclusion. The step length is 0.01 day.

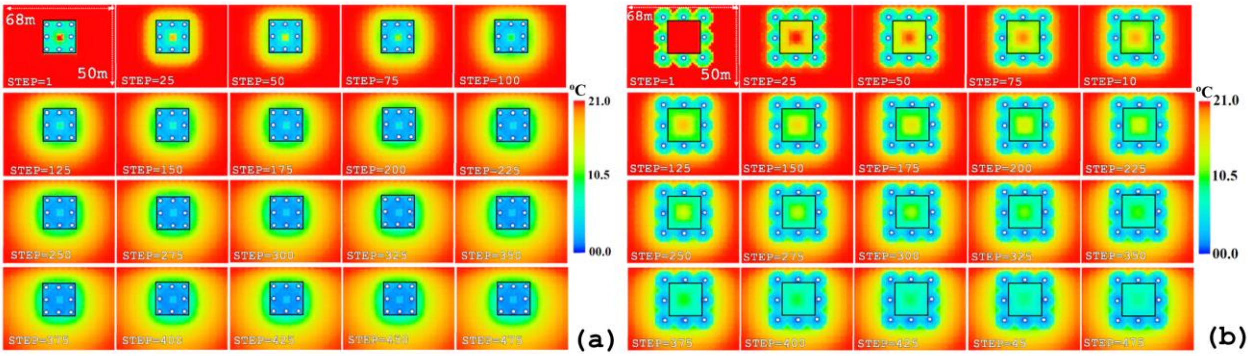

Fig. 16. Snapshot of thermal distribution inside Ottawa sand soil layer and square type Kaolin clay inclusion with $\varphi = 0.125$ when freezing pipes are installed a) inside inclusion; b) outside inclusion. The step length is 0.01 day.

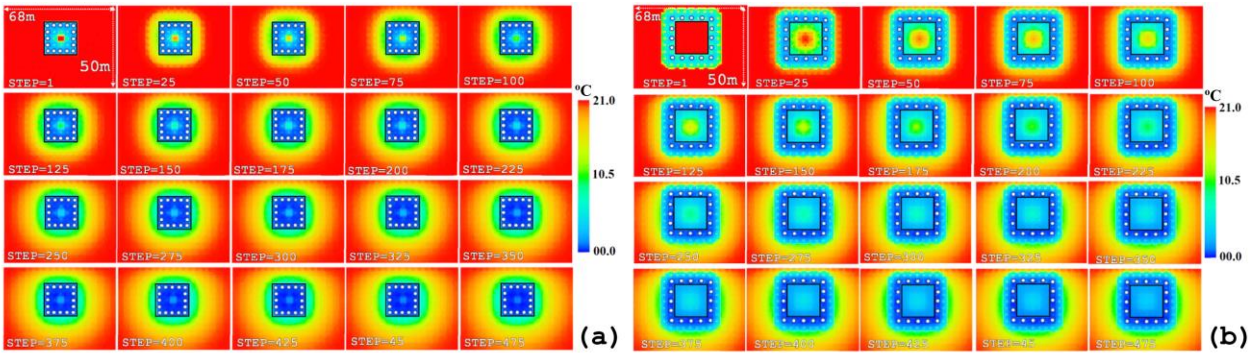

Fig. 17. Snapshot of thermal distribution inside Ottawa sand soil layer and square type Kaolin clay inclusion with $\varphi = 0.0625$ when freezing pipes are installed a) inside inclusion; b) outside inclusion. The step length is 0.01 day.

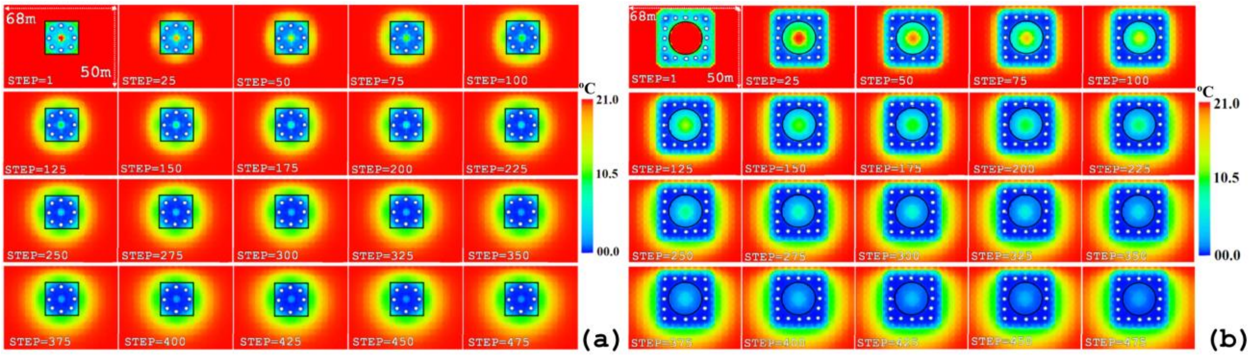

Fig. 18. Snapshot of thermal distribution inside Ottawa sand soil layer and Kaolin clay inclusion a) Square type inclusion-circular pipe configuration inside the inclusion, $\varphi = 0.120$; b) Circular type inclusion-square pipe configuration outside the inclusion, $\varphi = 0.0625$. The step length is 0.01 day.

4. Conclusion

In this paper, a hybrid boundary-finite element solution is proposed to study the freezing process in a nonhomogeneous soil layer containing circular and square-shaped inclusions. After presenting the boundary-finite element formulation and applying the method to the heat transfer equation, the discretized form of the equations is derived. The effects of inclusions within the soil layer were considered by introducing a substructure-subdomain method. Using this approach, the soil layer and inclusions were divided into two separate homogeneous models, and the hybrid method was then applied to each model. Furthermore, the equations obtained from each model were combined using continuity and consistency boundary conditions at the interface boundaries. The hybrid method and formulation were then implemented in a computer code called JMEL. After verifying the developed code by solving several classic examples and comparing the results with available analytical solutions, a parametric study was conducted. In this study, a soil layer with circular and square-shaped inclusions was modeled, and the temperature distribution at both interior and exterior points of the inclusions was evaluated. The results demonstrate that the proposed hybrid boundary-finite element method is highly effective for modeling heat transfer in soil layers containing arbitrarily shaped inclusions. This method can accurately predict freezing fronts in multilayer soils with complex geometries, making it a suitable numerical approach for soil improvement applications in geotechnical engineering. The main results of the parametric study can be summarized as follows:

- For freezing pipes installed inside the inclusion, the interior cools significantly (below 2 °C), but exterior temperatures remain relatively high, influenced by the surrounding soil's thermal properties. In sandy layers, temperatures decrease more rapidly and reach lower values compared to clay layers, highlighting the importance of soil characterization in thermal design.
- Sandy soils, due to their higher thermal diffusivity, can restrict freezing efficiency within clay inclusions. To mitigate this, increasing the number of freezing pipes outside the inclusion is recommended to enhance overall freezing performance.
- With pipes placed outside the inclusion, a larger freezing radius is achieved, improving exterior soil stabilization and yielding a more uniform interior temperature distribution. However, interior temperatures remain higher than when pipes are placed inside, a trade-off that should be considered based on uniformity versus intensity of cooling.
- The freezing growth pattern is predominantly governed by the arrangement of freezing pipes, not by the geometry of the inclusion. This suggests that pipe layout should be strategically planned to direct freezing fronts effectively, regardless of subsurface obstructions or inclusions.

- Optimal freezing performance, characterized by uniform temperature reduction and lower overall temperatures, is achieved when the freezing pipe configuration is aligned with the geometry of the inclusion. This alignment ensures efficient and predictable frost development tailored to the intended stabilization zone.

Despite the promising performance of the proposed hybrid boundary–finite element formulation, the present study is limited to single-phase heat transfer analysis with variable thermal conductivity. The phase change phenomenon associated with soil freezing was not explicitly modeled, and latent heat effects were not incorporated into the governing equations directly. Although this assumption simplifies the numerical implementation and provides reliable predictions for pre-freezing thermal behavior, accurate simulation of fully coupled freezing–thawing processes requires consideration of nonlinear phase change effects. Extending the proposed hybrid framework to incorporate enthalpy-based or Stefan-type phase change models represents an important direction for future research. Such an extension would enable more realistic modeling of moving freezing fronts and transient frost heave behavior in saturated soils.

From an engineering perspective, the developed method offers significant potential for practical applications in artificial ground freezing (AGF) projects, underground excavation support, tunnel shaft construction, groundwater control systems, and foundation stabilization in heterogeneous subsurface conditions. The capability of the method to efficiently model multilayer soils with inclusions of arbitrary geometry makes it particularly suitable for complex geotechnical environments where buried utilities, rock lenses, or structural obstructions are present. Therefore, the proposed approach provides a flexible and computationally efficient tool for thermal design and optimization of soil improvement systems in geotechnical engineering practice.

References

[1] Nicholson, P.G. (2015), Soil Improvement and Ground Modification Methods, Elsevier, Waltham, MA, USA, ISBN: 9780124080768.

[2] Andersland, O.B., Ladanyi, B. (1994), An Introduction to Frozen Ground Engineering, Springer Science-Business Media Dordrecht, Chapman & Hall, ISBN: 9781475722925.

[3] Casini, F., Gens, A., Olivella, S., Viggiani G.M.B. (2016), Artificial ground freezing of a volcanic ash: laboratory tests and modelling, Environmental Geotechnics, 3(3):141-154.

[4] Hu, J., Liu, Y., Li, Y., Yao, K. (2018), Artificial Ground Freezing in Tunnelling Through Aquifer Soil Layers: A Case Study in Nanjing Metro Line 2, KSCE Journal of Civil Engineering, 22:4136-4142.

[5] Joudieh, Z., Cuisinier, O., Abdallah, A., Masrouri, F. (2024), Artificial Ground Freezing—On the Soil Deformations during Freeze–Thaw Cycles, Geotechnics 4:718-741.

[6] Liu, Z., Sun, Y., Wang, B., Li, Q. (2020), Experimental Study of Artificial Ground Freezing by Natural Cold Gas Injection, Applied Sciences.,10:6055.

[7] Nikolaev, P., Jivkov, A.P., Margetts, L., Sedighi, M. (2024), Modelling artificial ground freezing subjected to high velocity seepage, International Journal of Heat and Mass Transfer, 221: 125084.

[8] Zhou, M.M., Meschke, G. (2014), Ground Improvement and Geosynthetics, Chapter: Numerical Modeling of Artificial Ground Freezing: Multiphase Modeling and Strength Upscaling, American Society of Civil Engineers, Pages: 209 – 219.

[9] Alzoubi, M., Xu, M., Hassani, F., Poncet, S., Sasmito, A.P. (2020), Artificial ground freezing: A review of thermal and hydraulic aspects, Tunnelling and Underground Space Technology, 104:103534.

[10] Ren, Zh., Liu, J., Jiang, H., Wang, E. (2023), Experimental study and simulation for unfrozen water and compressive strength of frozen soil based on artificial freezing technology, Cold Regions Science and Technology, 205:103711.

[11] Williams, M., Saberi, M., Meschke, G. (2024), Numerical investigation of artificial ground freezing–thawing processes in tunnel construction, Computers and Geotechnics, 173: 106477.

[12] Kamalian, M., Jafari, M.K., Sohrabi-Bidar, A., Razmkhah, A., Gatmiri, B. (2006), Time-domain two-dimensional site response analysis of non-homogeneous topographic structures by a hybrid BE/FE method, Soil Dynamics and Earthquake Engineering, 26: 753-765.

[13] Lienhard IV, J.H., Lienhard V, J.H. (2008), A Heat Transfer Textbook, Third Edition, Cambridge, Massachusetts, USA.

[14] Brebbia, C.A., Dominguez, J. (1992), Boundary Elements an Introductory Course, Computational Mechanics Publications, ISBN: 1562520873.

[15] Logan, D.L. (2007), A First Course in the Finite Element Method, Fourth Edition, ISBN: 0534552986.

[16] Partridge, P.W., Brebbia, C.A. (1990), Computer implementation of the BEM dual reciprocity method for the solution of general field equations, Communications in Applied numerical methods, 6: 83-92.

[17] Dominguez, J. (1993), Boundary Element in Dynamics, Computational Mechanics Publications, ISBN: 1562521829.

[18] Burden, R.L., Faires, J.D. (2011), Numerical Analysis, Ninth Edition, Boston, USA, ISBN: 139780538733519.

[19] Newmark, N.M. (1959), A Method of Computation for Structural Dynamics. Journal of the Engineering Mechanics Division, 85(3): 67-94.

[20] Johnson, D.E. (1996), A Proof of the Stability of the Houbolt Method. American Institute of Aeronautics and Astronautics, 4(8): 1450-1451.

[21] Bruch, J.C., Zyvoloski, G. (1974), Transient Two-dimensional Heat Conduction Problems Solved by the Finite Element Method, International Journal for Numerical Methods in Engineering, 8:481-494.

[22] Wrobel, L.C., Brebbia, C.A., Nardini, D. (1986), The Dual Reciprocity Boundary Element Formulation for Transient Heat Conduction, in Finite Elements in Water Resources VI, Computational Mechanics Publications, Southampton and Springer-Verlag, Berlin and New York.

[23] Wrobel, L.C., Telles, J.C.F., Brebbia, C.A. (1986), A Dual Reciprocity Boundary Element Formulation for Axisymmetric Diffusion Problems, in Boundary Elements VIII, Vol. 1, Computational Mechanics Publications, Southampton and Springer-Verlag, Berlin and New York.

[24] Carpenter, T. (2019), Thermal Properties of Dry and Saturated Soils, Master’s Thesis, University of Tennessee, Knoxville, USA.

[25] Bonacina, C., Comini, G., Fasano, A., Primicerio, M. (1973), Numerical solution of phase-change problems, International Journal of Heat and Mass Transfer, 16(10): 1825-1832.